Frequency Effects of Upstream Wake and Blade Interaction on the Unsteady Boundary Layer Flow

Dong Jin Kang*, Sang Su Bae
School of Mechanical Engineering, Yeungnam University, Kyungbuk 712-749, Korea

Effects of the reduced frequency of upstream wake on downstream unsteady boundary layer flow were simulated by using a Navier-Stokes code. The Navier-Stokes code is based on an unstructured finite volume method and uses a low Reynolds number turbulence model to close the momentum equations. The geometry used in this paper is the MIT flapping foil experimental set-up and the reduced frequency of the upstream wake is varied in the range of 0.91 to 10.86 to study its effect on the unsteady boundary layer flow. Numerical solutions show that they can be divided into two categories. One is so called the low frequency solution, and behaves quite similar to a Stokes layer. Its characteristics is found to be quite similar to those due to either a temporal or spatial wave. The low frequency solutions are observed clearly when the reduced frequency is smaller than 3.26. The other one is the high frequency solution. It is observed for the reduced frequency larger than 7.24. It shows a sudden shift of the phase angle of the unsteady velocity around the edge of the boundary layer. The shift of phase angle is about 180 degree, and leads to separation of the boundary layer flow from corresponding outer flow. The high frequency solution shows the characteristics of a temporal wave whose wave length is half of the upstream frequency. This characteristics of the high frequency solution is found to be caused by the strong interaction between unsteady vortices. This strong interaction also leads to destroy of the upstream wake strips inside the viscous sublayer as well as the buffer layer.

Key Words: Unsteady Boundary Layer Flow, MIT flapping foil, Reduced Frequency, Traveling Wave, Frequency Effects

1. Introduction

Unsteady boundary layer flows occur in many different applications such as an airfoil subjected to a gust stream, marine propulsor and hull interaction, rotor-stator interaction in turbomachinery etc. They can be classified as one of three types such as spatial, temporal, or traveling wave in accordance with the cause of unsteadiness. Even though a number of papers were published since early 70s, their characteristics are not fully understood yet. Futhermore, most of previous studies are for a flat plate subjected to a uniform stream with a temporal wave superimposed.

The unsteady boundary flow due to a temporal wave has been most widely studied. For example, Tsahalis and Telionis (1981) studied a periodic Howarth flow with a superimposed temporal wave. The responses are characterized by overshoot of the Stokes layer and lead of phase angle of the skin friction by about 45 degree when the reduced frequency $k=\omega c/2V_\infty$ is greater than 1.0. Here, ω, c, and V_∞ are frequency, characteristic length and free stream velocity, respectively. A similar stokes layer is also observed in the spatial wave case. For example, Stern and his students (Stern et al., 1989; Choi et al., 1996) found that the unsteady boundary layer due to a spatial wave

* Corresponding Author.
E-mail : djkang@yu.ac.kr
TEL : +82-53-810-2463; FAX : +82-53-813-3703
Associate Professor, School of Mechanical Engineering, Yeungnam University, Gyongsan, Kyungbuk 712-749, Korea. (Manuscript Received August 28, 2001; Revised July 18, 2002)

shows the Stokes layer behavior. But, the amplitude of the Stokes layer is much larger than that of temporal wave case, and nonlinear interaction between mean and first harmonic velocity components is observed much stronger.

The unsteady boundary layer due to a traveling wave is the least studied case. The traveling wave can be one of horizontal, vertical or combined wave. Unlike other wave disturbances, the traveling wave case is known to show larger unsteady fluctuation of lift. For example, the MIT experiment (Horwich, 1993) of flapping foil and hydrofoil interaction and the related computations (Lee, et al., 1995 ; Paterson and Stern, 1999) show that the unsteady fluctuation is about 15% of the static lift. Furthermore, the high reduced frequency (wave length shorter than the foil chord) solutions deviate much from the classical inviscid flow theory as Paterson and Stern (1999) showed. They attributed the viscous-inviscid interaction to a major deriving mechanism for the unsteady fluctuation of lift and oscillation of wake sheet. The resulting unsteady boundary layer flow due to a traveling wave is also known to be much more complex than due to other waves.

The MIT experiment was conducted extensively to get very detailed unsteady boundary layer data due to a traveling wave. For example, Horwich (1993) made an elaborate measurement to provide unsteady data of good quality for the reduced frequency of 3.62. The geometry of the MIT experiment is therefore chosen to use in this paper. The MIT experimental geometry consists of 2 flapping foils and a fixed hydrofoil as shown in Fig. 1. The reduced frequency is however varied in a fairly wide range of 0.91 to 10.86 to study effects of the reduced frequency. This range of the reduced frequency is much wider than in any of previous studies. Paterson and Stern (1999) carried out a similar computational study. But, they used a potential flow model instead of the upstream flapping foils. So, a smaller domain enclosing only the hydrofoil was simulated. On the contrary, the present study simulates the whole geometry of the MIT flapping foil experiment and does not need to use any

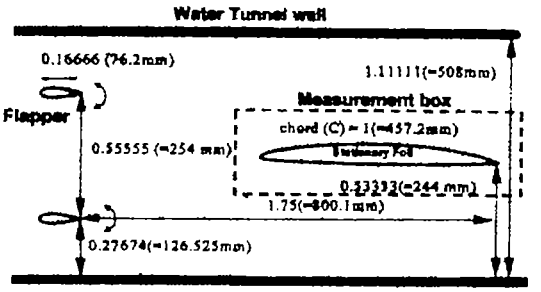

Fig. 1 Schematic diagram of the MIT flapping foil experiment

model for the upstream wake. The angle of the flapping motion of the upstream foils is kept constant at 6 degree to isolate effects of the reduced frequency.

2. Governing Equations

The Reynolds-averaged Navier-Stokes equations in a moving coordinate system for two-dimensional unsteady incompressible flows can be written as :

$$\frac{\partial u}{\partial t}+u\frac{\partial u}{\partial x}+v\frac{\partial u}{\partial y}-\frac{\partial x}{\partial t}\frac{\partial u}{\partial x}-\frac{\partial y}{\partial t}\frac{\partial u}{\partial y}=-\frac{1}{\rho}\frac{\partial p}{\partial x}+\nu_{eff}\left(\frac{\partial^2 u}{\partial x^2}+\frac{\partial^2 u}{\partial y^2}\right) \tag{1}$$

$$\frac{\partial v}{\partial t}+u\frac{\partial v}{\partial x}+v\frac{\partial v}{\partial y}-\frac{\partial x}{\partial t}\frac{\partial v}{\partial x}-\frac{\partial y}{\partial t}\frac{\partial v}{\partial y}=-\frac{1}{\rho}\frac{\partial p}{\partial y}+\nu_{eff}\left(\frac{\partial^2 v}{\partial x^2}+\frac{\partial^2 v}{\partial y^2}\right) \tag{2}$$

$$\frac{\partial u}{\partial x}+\frac{\partial v}{\partial y}=0 \tag{3}$$

where the terms involving $\partial x/\partial t$ or $\partial y/\partial t$ are due to the movement of grid points. The effective viscosity ν_{eff} is defined as $\nu_{eff}=\nu+\nu_t$, and eddy viscosity ν_t is modelled from the low Reynolds number $\kappa-\varepsilon$ turbulence model of Chien (1982).

The low Reynolds turbulence model of Chien (1982) determines the turbulence kinetic energy k and its dissipation rate ε from the following transport equations :

$$\frac{\partial \kappa}{\partial t}+\frac{\partial u_j \kappa}{\partial x_j}=\frac{\partial x_j}{\partial t}\frac{\partial \kappa}{\partial x_j}=\frac{1}{\rho}\frac{\partial}{\partial x_j}\left[\left(\mu+\frac{\mu_t}{\sigma_\kappa}\right)\frac{\partial \kappa}{\partial x_j}\right]+\frac{\mu_t}{\rho}\left(\frac{\partial u_i}{\partial x_j}+\frac{\partial u_j}{\partial x_i}\right)\frac{\partial u_j}{\partial x_i}-\varepsilon-\frac{2\nu\kappa}{y^2} \quad (4)$$

$$\frac{\partial \varepsilon}{\partial t}+\frac{\partial u_j \varepsilon}{\partial x_j}=\frac{\partial x_j}{\partial t}\frac{\partial \varepsilon}{\partial x_j}=\frac{1}{\rho}\frac{\partial}{\partial x_j}\left[\left(\mu+\frac{\mu_t}{\sigma_\varepsilon}\right)\frac{\partial \varepsilon}{\partial x_j}\right]+f_1 C_{\varepsilon 1}\frac{\mu_t}{\rho}\left(\frac{\partial u_i}{\partial x_j}+\frac{\partial u_j}{\partial x_i}\right)\frac{\partial u_j}{\partial x_i}-C_{\varepsilon 2}f_2\frac{\varepsilon^2}{\kappa}-2\varepsilon\nu\frac{e^{-0.5y^+}}{y^2} \quad (5)$$

where model constants $C_{\varepsilon 1}$, $C_{\varepsilon 2}$, C_μ, σ_k, and σ_ε are defined as 1.35, 1.8, 0.09, 1.0, and 1.3, respectively. Model functions f_μ, f_1, and f_2 are defined as $1-e^{-0.0115y^+}$, 1.0, and $1-2.2e^{-\frac{R_t^2}{36}}$, respectively. Here, y^+ and R_t are defined as $\frac{y\sqrt{\frac{\tau_w}{\rho}}}{\nu}$ and $\frac{\kappa^2}{\nu\varepsilon}$. τ_w stands for wall shear stress. The turbulence viscosity ν_t is represented as $C_\mu f_\mu \frac{\kappa^2}{\varepsilon}$.

3. Numerical Solution Method

The present Navier-Stokes code is based on the unstructured grid finite volume method which was developed by the authors in a previous study (Kang and Bae, 1998). We have extended the unstructured grid Navier-Stokes procedure for incompressible flows developed by Thomadakis et al. (1996) to allow collocated storage of all variables. Since Thomadakis et al. (1996) used a staggered grid formulation, pressure is stored at the centroid of a cell while velocity components are stored at grid points. We modified this procedure to allow non-staggered storage in the same way as being done for structured grid methods (Kang and Bae, 1998).

The present unstructured grid Navier-Stokes code uses momentum equations written in physical coordinates (x, y), and a pressure equation is derived by substituting the discretized momentum equations into the continuity equation. The process of deriving the pressure equation is almost the same as for structured grid methods. The present Navier-Stokes code uses the QUICK scheme for the convective terms and the second order Euler backward difference for time derivatives to keep second order accuracy.

4. Moving Grid

The MIT experiment set up consists of two upstream flapping airfoils and one stationary downstream hydrofoil : two upstream airfoils are flapping at a given reduced frequency. To accurately simulate the motion of the flapping airfoils, a mixed grid system of structured and unstructured meshes is used as shown in Fig. 2. Grids around the flapping airfoils, hydrofoil and tunnel walls are structured while the remaining domain is meshed with an unstructured grid method. The structured O-type grid around the airfoils are flapping with the corresponding airfoils at a reduced frequency. The grid points on the boundary between structured and unstructured grid points are therefore moving, and reconstruction of finite volumes for the grid points on this boundary is required at each time step. Figure 3 explains how this need is satisfied. Suppose a grid system (solid lines) around a flapping airfoil at time $t=t_1$ is moved to another grid system (dashed line) at later time $t=t_2$. So, all grid points on the right of the boundary Γ are rotated, and all finite volumes containing any grid point on the boundary Γ should be reconstructed. For example, grid point i_1 is moved to i_1'. Then a new finite volume after rotation is formed by connecting 4 nearest neighboring grid points, j_1, j_2, i_1, i_2. As this reconstruction process is quite simple, computational overhead due to the present moving grid technique is negligibly small.

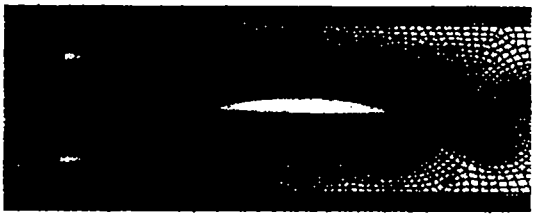

Fig. 2 Computational domain and grid

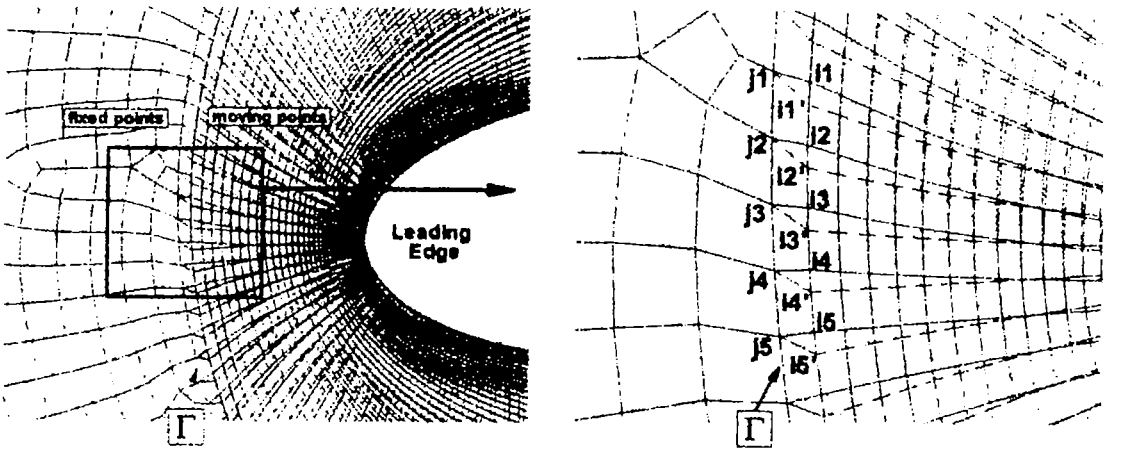

(a) Grid movement (b) Grid at time $t=t_2$

Fig. 3 Moving grid technique

5. Code Validation

It is necessary to validate the present Navier-Stokes code and study spatial and temporal grid sensitivity before an elaborate numerical experiment. The code validation was made at the Reynolds number, based on the hydrofoil chord length and average velocity in the water tunnel, of 3.78×10^6. At inlet boundary, turbulence intensity was assumed as 1% as suggested by Rice (1991). Uniform axial velocity and Neumann condition for pressure were set at the inlet boundary. Neumann conditions for all dependent variables were used at the outlet boundary.

Two different number of computational grid points were used to see spatial grid sensitivity: case 1 with 43,588 grid points and case 2 with 35,988. A typical grid distribution is shown in Fig. 2. Effect of time step size was also checked by comparing two numerical solutions, one obtained for a time step size of $\Delta t=T/200$ and the other for $\Delta t=T/400$. Here T is the period of the flapping airfoils. Figure 4(a) compares three numerical solutions against each other and also with the experimental data in terms of the pressure coefficient distribution along the surfaces of the hydrofoil. All three numerical solutions show good agreement with each other as well as the experimental data. Figure 4(b) shows the effect of

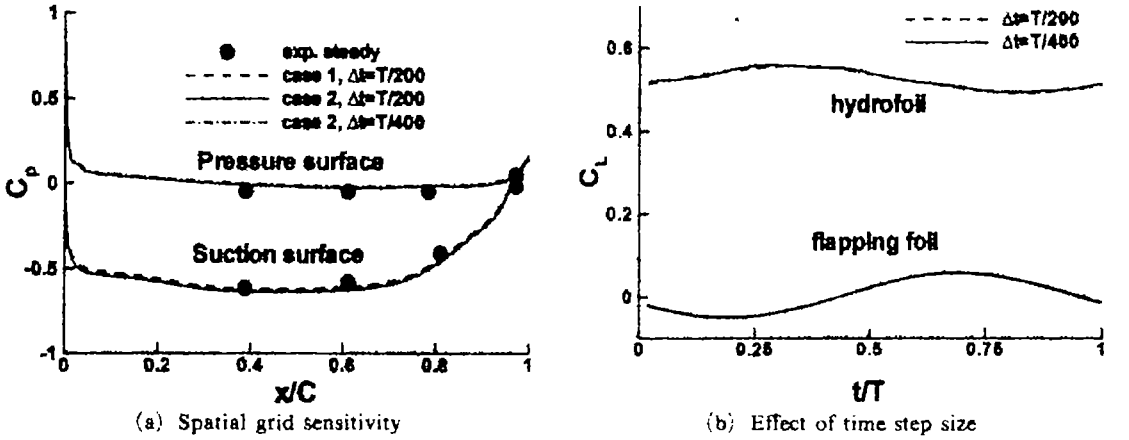

(a) Spatial grid sensitivity (b) Effect of time step size

Fig. 4 Accuracy of numerical solutions (● : experiment by Horwich E. A.)

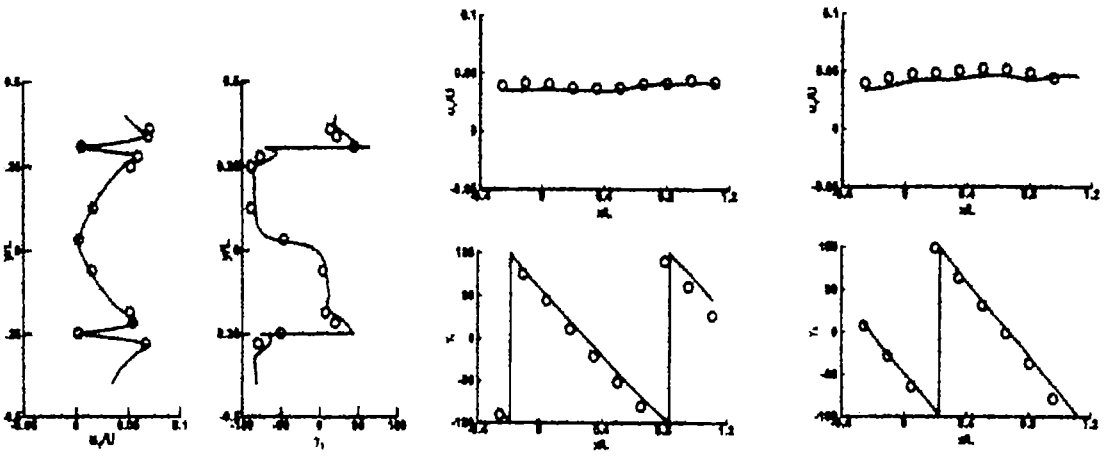

(a) Inlet boundary (b) Top boundary (c) Bottom boundary

Fig. 5 Comparison of the first harmonic of the axial velocity components on the measurement box (○ : experiment by Horwich E. A., ——— : present)

time step size on the unsteady lift variation of the hydrofoil. These lift variations were obtained after marching 5 periods. Two solutions show a negligible difference between them. Figure 5 shows a comparison of the first harmonic of the velocity components along the boundary of the measurement box shown in Fig. 1. All present solutions of magnitude and phase angle show good agreement with the corresponding experimental data, better than previous numerical solutions (Lee et al., 1995 ; Paterson et al., 1999). More detailed comparisons can be found in Kang and Bae (1999a). These preliminary computations confirm that computations with 43,588 grid points and a time step size of $\Delta t = T/400$ would accurately simulate the steady and unsteady flow characteristics of the MIT experiment. So, all computations reported in this paper were carried out with a time step size of $\Delta t = T/400$ and 43,588 grid points.

6. Results and Discussions

To study effects of the reduced frequency, computations have been carried out for the reduced frequency in the range of 0.96 to 10.86. Here, the reduced frequency of 3.62 is the case for which a thorough code validation was made.

Figure 6 shows the wake from the flapping airfoils in terms of the first harmonics of the unsteady velocity components for 4 reduced frequencies of 0.91, 3.62, 7.24 and 10.86. The unsteady velocity was calculated by subtracting time averaged value from the instantaneous velocity at each time step. All profiles in Fig. 6 were drawn at the left side of the measurement box shown in Fig. 1. The amplitude of the first harmonics of the unsteady velocity show great dependency on the reduced frequency. The amplitude of v_1, the first harmonics of v, increases monotonically with increase of the reduced frequency, while the amplitude of u_1 remains nearly constant for the reduced frequency larger than about 3.62. Comparison with the potential flow model used by Paterson et al. (1999) shows that the potential flow model is valid only in a much smaller region than they expected.

Figure 7 shows the first harmonics of the surface pressure coefficient for 4 reduced frequencies of 0.91, 3.62, 7.24 and 10.86. One typical behavior of the harmonics is that its very large fluctuation near the leading edge declines as approaching the trailing edge, with one or two humps depending on the frequency. But, this typical behavior is not observed anymore when the reduced frequency is larger than 7.24. In stead, the magnitude of the first harmonics is almost constant. This totally different figure reflects that

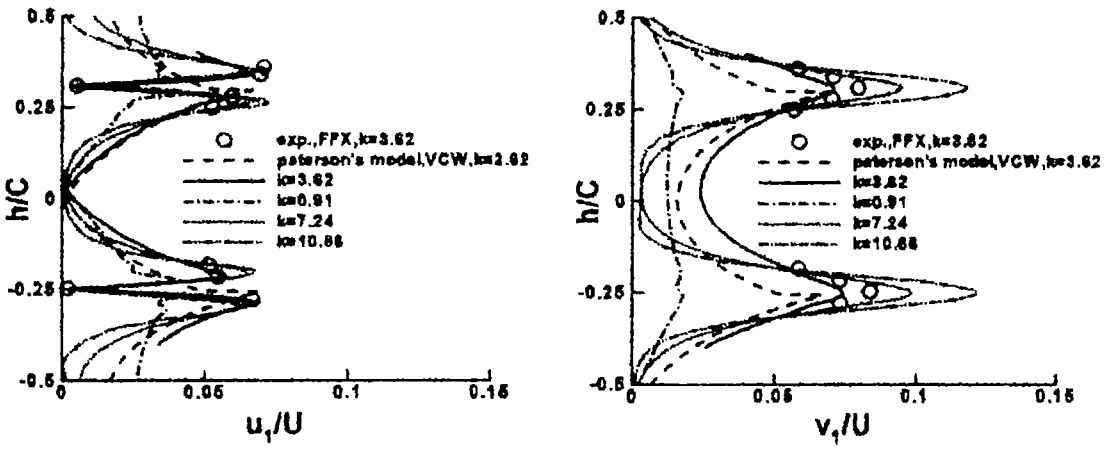

(a) Magnitude of the first harmonic u-velocity (b) Magnitude of the first harmonic v-velocity

Fig. 6 Comparison of the first harmonic of the MIT flapping foil wake for reduced frequencies (○ : experiment by Horwich E.A.)

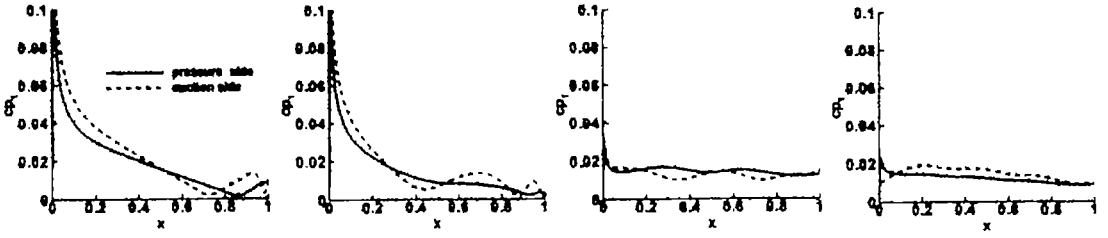

(a) k=0.91 (b) k=3.62 (c) k=7.24 (d) k=10.86

Fig. 7 Comparison of the first harmonic of Cp

the characteristics of the unsteady boundary layer flow changes drastically when the reduced frequency is larger than about 7.24.

Another change in the characteristics of the unsteady boundary layer flow is seen in Fig. 8 which shows the first harmonics of the unsteady velocity profiles at several axial locations. For the reduced frequency less than 2.72, the first harmonic component of the unsteady velocity profile behaves quite similar to the Stokes layer observed in the case of a temporal wave. The phase angle shift of the boundary layer flows from the free stream is about from 30 to 90°, depending on x/c as can be seen in Fig. 8(a), (b), (c) and (d). The phase angle shift also seems quite smooth and increases as approaching the wall. This figure is, however, changed drastically for the high frequency solutions ($k \geq 7.24$). They show sudden change of the phase angle around the edge of boundary layer. The amount of the sudden phase angle shift is nearly 180 degree as can be seen in Fig. 8(c) and (d). This sudden phase angle shift also leads to the cancellation of the unsteady fluctuation near the edge of boundary layer as can be seen in Figs. 8(e) ~ (h). A very similar behavior (abrupt change of phase angle, larger phase angle lead, and local recession of the first harmonic) was also observed by Choi et al. (1996) in the laminar boundary layer flows with traveling wave external flows. Paterson et al. (1999) had reported a similar behavior for the turbulent boundary layer flows.

The sudden shift of the phase angle and the cancellation of unsteady fluctuation near the boundary layer edge seem as the most prominent characteristics of the high frequency solutions. Furthermore, they cause the unsteady boundary layer to behave nearly independent of the outer flow. This separation is obviously observed in time history of turbulent kinetic energy. Figure 9

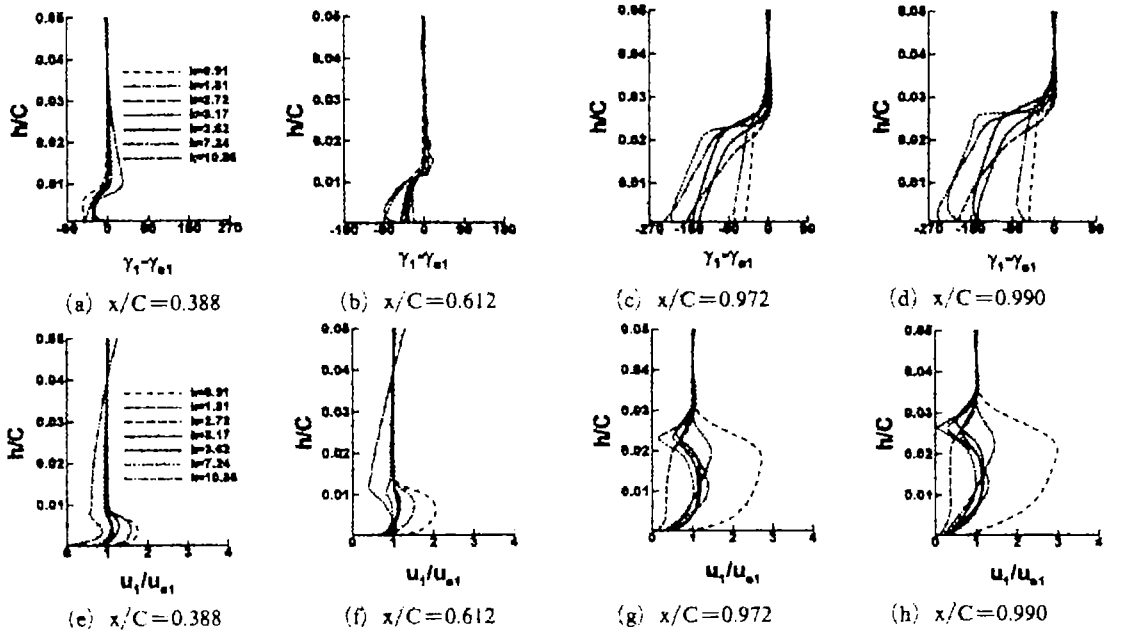

(a) x/C=0.388 (b) x/C=0.612 (c) x/C=0.972 (d) x/C=0.990

(e) x/C=0.388 (f) x/C=0.612 (g) x/C=0.972 (h) x/C=0.990

Fig. 8 Magnitude and phase angle of the first harmonics of the velocity profiles at several location along the surface of the hydrofoil

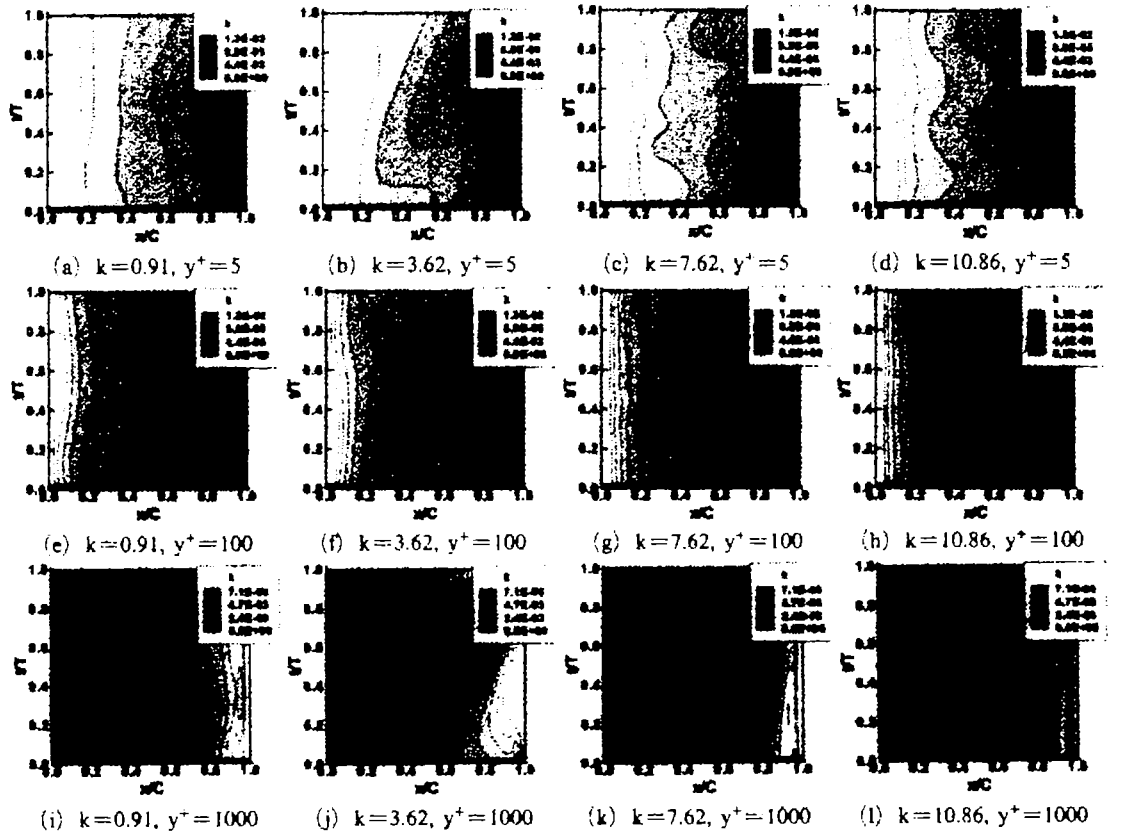

(a) k=0.91, y^+=5 (b) k=3.62, y^+=5 (c) k=7.62, y^+=5 (d) k=10.86, y^+=5

(e) k=0.91, y^+=100 (f) k=3.62, y^+=100 (g) k=7.62, y^+=100 (h) k=10.86, y^+=100

(i) k=0.91, y^+=1000 (j) k=3.62, y^+=1000 (k) k=7.62, y^+=1000 (l) k=10.86, y^+=1000

Fig. 9 Time history of the turbulence kinetic energy for four frequencies

shows the time history of the turbulent kinetic energy at 3 normal distances from the wall for 4 reduced frequencies of 0.91, 3.62, 7.26, and 10.86. When the reduced frequency is less than or equal to 3.62, the upstream wakes are observed even in the laminar sublayer. But, in the case of the reduced frequencies 7.26 and 10.86, the upstream wake trajectories are completely destroyed inside both the inner and buffer layers. A very similar behavior is also observed in the distribution of the unsteady velocity (not shown in this paper). This particular behavior is another characteristics of the high reduced frequency solution.

Figures 10 and 11 respectively show the unsteady turbulent kinetic energy and temporal variation of the unsteady velocity at 3 normal positions from the wall for several reduced frequencies and 3 axial locations. The low frequency solution for k=0.91 show a simple sinusoidal variation with the wave length T the same as the outer unsteady flow, while the responses of the high frequency solution for k=10.86 have a wave length of about T/2 inside the boundary layer. This difference of wave length is another characteristics of the high reduced frequency solution. Figure 12 shows temporal variation of surface pressure coefficient. The low frequency solution for k=0.92 clearly shows a sinusoidal response in

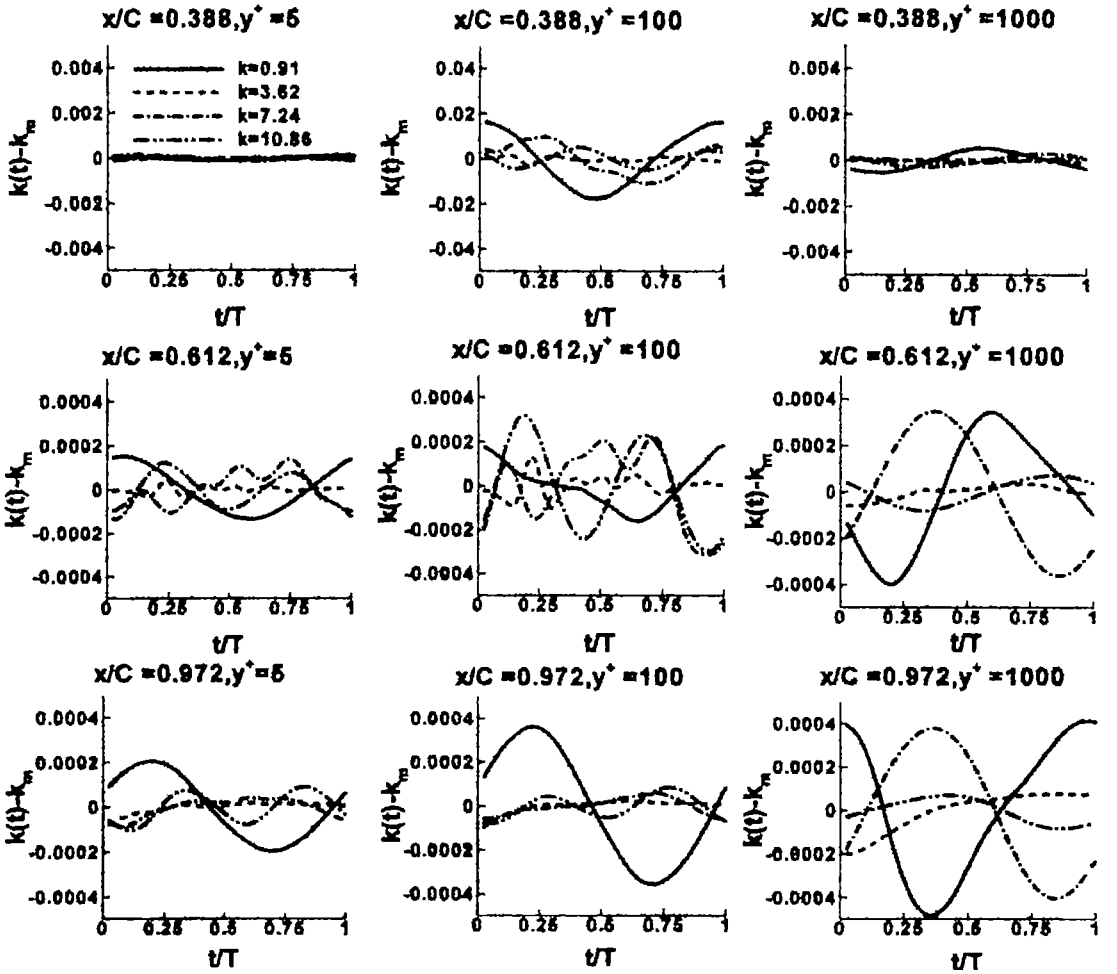

Fig. 10 Time history of the unsteady turbulence kinetic energy at 3 normal positions from the suction surface of the hydrofoil

all figures, while the high frequency solution for k=10.86 shows again a wave of length T/2. The wave length T/2 of the high frequency solution is a very interesting phenomenon.

Figure 13 shows temporal evolutions of the unsteady velocity field at 4 normal positions from the wall. The temporal evolutions were obtained by slicing the velocity field, along the surface of the hydrofoil, at certain normal distance from the wall. Since two consecutive unsteady vortices rotates in reverse, the boundary between two unsteady vortices appears as a strip. So 4 wide strips in Fig. 13(d) indicate that 4 unsteady vortices travel along the surface of the hydrofoil. Other narrow strips between two consecutive strips are roughly trajectories of the centers of unsteady vortices. One interesting observation is that the temporal evolutions of the unsteady vortices show great distortion due to the interaction between them as going down toward the wall. The distortion of the traveling wave is so strong that it eventually develops into a temporal wave of length T/2 as shown in Fig. 13(a). This is why the unsteady velocity at $y^+=5$ for k=10.86 shows the behavior of a temporal wave of length T/2 as can seen in Fig. 11. Figs. 13(b) and (c) show distorted traveling waves. The development of the traveling wave into a temporal wave inside the boundary layer is powered by temporal pressure gradient whose wave length is T/2 as

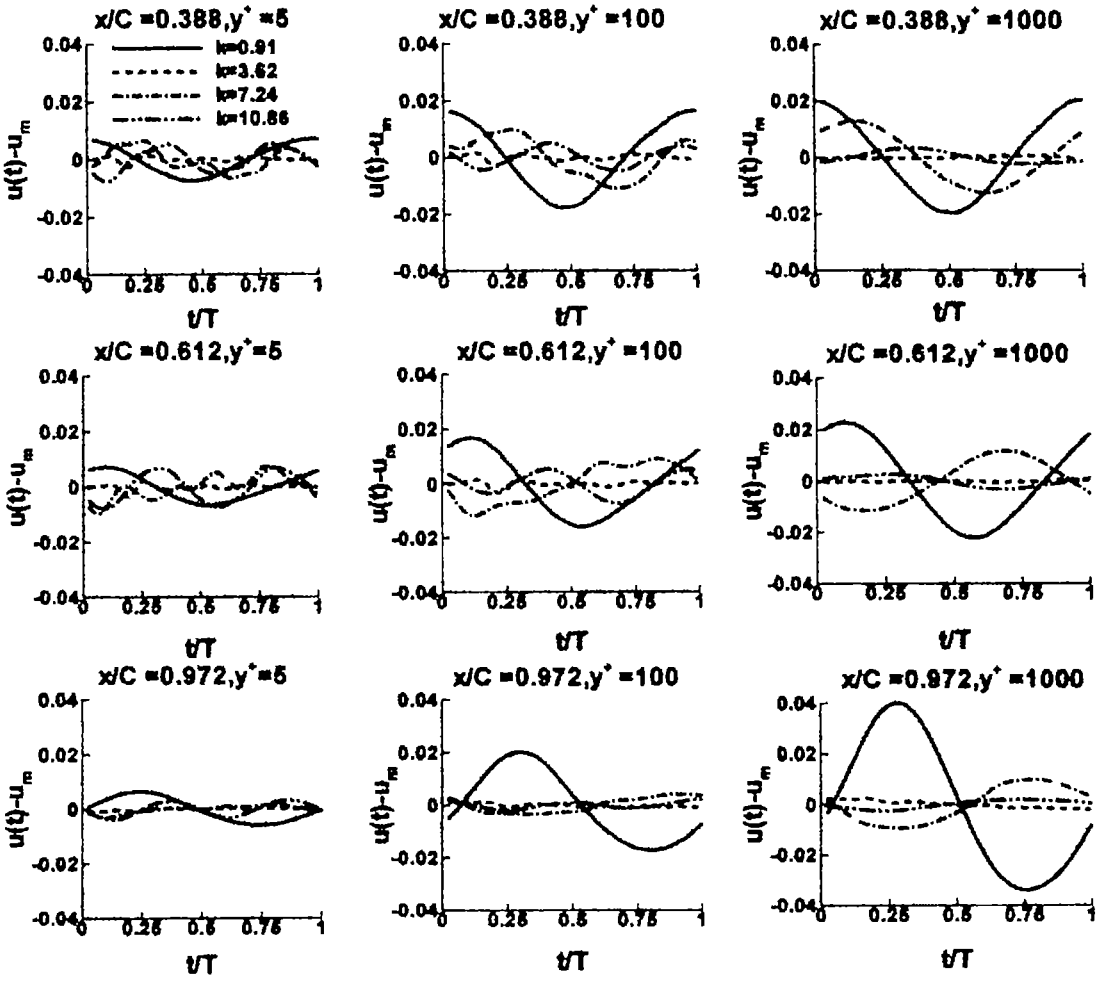

Fig. 11 Time history of the unsteady velocity at 3 normal positions from the suction surface of the hydrofoil

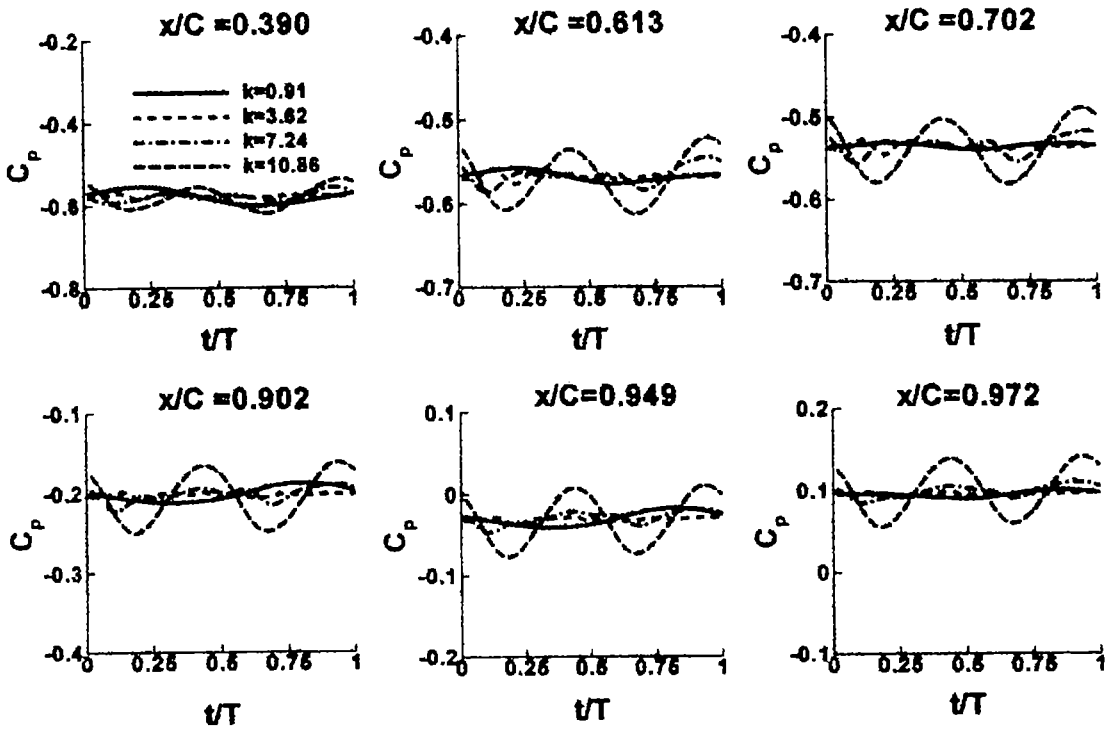

Fig. 12 Time history of the surface pressure coefficient

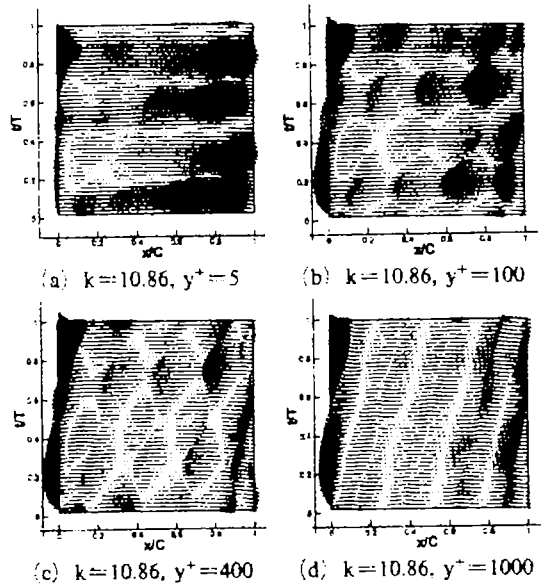

(a) k=10.86, y^+=5 (b) k=10.86, y^+=100

(c) k=10.86, y^+=400 (d) k=10.86, y^+=1000

Fig. 13 Time history of the unsteady velocity field at 3 normal positions from the suction surface of the hydrofoil

7. Conclusions

The MIT flapping foil experimental set-up was simulated to study the effects of the reduced frequency of the upstream wake on the downstream unsteady boundary layer. Computations have been carried out for the reduced frequency in the range of 0.91 to 10.86, with the angle of flapping motion kept constant at 6 degree.

The unsteady boundary layer flows due to a traveling wave are shown to have different characteristics according to the magnitude of the reduced frequency. One is called the low reduced frequency solution. It behaves similar to the Stokes layer which is observed in the unsteady boundary layer due to either of a temporal or a spatial wave. The other one is the high reduced frequency solution. It shows sudden change of the phase angle of the unsteady velocity near the edge of boundary layer. This phase angle shift weakens the interaction between free stream and corresponding boundary layer flows. Consequen-

shown in Fig. 12.

tly the unsteady boundary layer flow becomes almost independent of the outer flow conditions. The temporal evolutions of the turbulent kinetic energy and unsteady velocity show temporal waves of length T/2 inside the boundary layer, while they are traveling waves of length T in the free stream. The wave length of T/2 is derived by a temporal pressure gradient. The nonlinear interaction between unsteady vortices also promotes the traveling waves to develop into temporal waves of length T/2.

Acknowledgment

This study was supported by the Korea Science and Engineering Foundation through the Regional Research Center for Advanced Climate Control Technology at Sun Moon University and the Brain Korea 21 Project of Yeung Nam University.

References

Choi, J. E., Sreedhar, M. K., Stern, F., 1996, "Stokes Layers in Horizontal Wave Outer Flows," ASME J. Fluids Engineering, Vol. 118, pp. 537-545.

Gissing, J. P., 1969, "Vorticity and Kutta Condition for Unsteady Multi-Energy Flow," *ASME J. Applied Mechanics*, Vol. 36, pp. 608~613.

Horlock, J., 1968, "Fluctuating Lift Forces on an Airfoils Moving through Transverse and Chordwise Gusts," *ASME J. Basic Engineering*, pp. 494~500.

Horwich, E. A., 1993, "Unsteady Response of a Two Dimensional Hydrofoil Subject to High Reduced Frequency Gust Loading," M. S. Thesis, Dept. of Ocean Eng., MIT, Cambridge, MA.

Kang, D. J., Bae, S. S., and Joo, S. W., 1998, "An Unstructured FVM for the Numerical Prediction of Imcomressible Viscous Flows," *Transactions of the KSME*, Vol. 22, No. 10, pp. 1410~1421.

Kang, D. J., Bae, S. S., 1999a, "Navier-Stokes Simulation of MIT FFX by Using an Unstructured Finite Volume Method," *ASME Turbo -Expo* IGTI-99-214.

Lee, Y. T., Kirtis, C., Rogers, S. E., Zawadzki, I. and Kwak, D., 1995, "Steady and Unsteady Multi-Foil Interactions by Navier-Stokes and Euler Calculations," *Unsteady Aerodynamics and Aeroelasticity of Turbomachines*, Elsevier Science, pp. 93~107.

Paterson, E. G. and Stern, F., 1999, "Computation of Unsteady Viscous Marine Propulsor Blade Flows-Part 2: Parametric Study," *ASME J. Fluids Engineering*, Vol. 121, pp. 121~147.

Poling, D. R. and Telionis, D. P., 1986, "The response of Airfoils to Periodic Disturbances-The Unsteady Kutta Condition," *AIAA J.* Vol. 24, No. 2, pp. 193~199.

Rice, J. Q., 1991, "Investigation of Flows around a Two-dimensional Hydrofoil in Steady and Unsteady Flows," M. S. Thesis, Dept. of Ocean Eng., MIT, Cambridge, MA.

Tsahalis, D. Th. and Telionis, D. P., 1974, "Response of Separation to Impulsive Changes of Outer Flow," *AIAA J.* Vol 12, pp. 614~619.

Thomadakis, M. and Leschziner, M., 1996, "A Pressure Corection Method for the Solution of Incompressible Viscous Flows on Unstructured Grids," *Int. J. Nume. Methd. in Fluids*, Vol. 22, pp. 581~601.

Stern, F., Hwang, W. S. and Jaw, S. Y., 1989, "Effects of Waves on the Boundary Layer of Surface Piercing Flat Plate: Experiment and Theory," *J. Ship Research*, Vol. 33, pp. 63~68.